Supporting Information

Zn vacancy-anchored Ag clusters on single-unit-cell $ZnIn_2S_4$ nanosheets for efficient dual-function photocatalysis

Lifang Yang [a,1], Yuge Zhang [b,1], Yong Liu [c,*], Zhijun Yang [a], Guanghui Li [a], Jianwei Zhou [a], Sugang Meng [b,*], Raf Dewil [c,d]

[a] School of Chemistry and Materials Engineering, Xinxiang University, Xinxiang 453000, China.

[b] Key Laboratory of Green and Precise Synthetic Chemistry and Applications, Ministry of Education; School of Chemistry and Chemical Engineering, Huaibei Normal University, Huaibei, 235000, China.

[c] KU Leuven, Department of Chemical Engineering, Chemical and Biochemical Reactor Engineering and Safety, J. De Nayerlaan 5, 2860 Sint-Katelijne-Waver, Belgium.

[d] University of Oxford, Department of Engineering Science, Parks Road, Oxford OX1 3PJ, United Kingdom.

[*] Corresponding authors, E-mail: liuyong0781@outlook.com (Y. Liu); sgmeng@chnu.edu.cn (S. Meng).

[1] These authors contributed equally to this paper.

Test S1. Materials

Indium chloride tetrahydrate ($InCl_3 \cdot 4H_2O$, 99.9%), zinc acetate dihydrate ($Zn(CH_3COO)_2 \cdot 2H_2O$, ≥99%), thioacetamide ($C_2H_5NS$, 99.0%), and silver nitrate ($AgNO_3$, ≥98%) were purchased from Sinopharm Chemical Reagent Co., Ltd. Benzyl alcohol ($C_6H_5CH_2OH$, ≥99.0%), triethanolamine ($C_6H_{15}NO_3$, ≥99.0%), sodium sulfate (Na_2SO_4, ≥98.0%), potassium chloride (KCl, 99.8%), ethanol (C_2H_5OH, 99.5%), potassium ferricyanide ($K_3FeC_6N_6$, 99.0%), potassium ferrocyanide trihydrate ($K_4FeC_6N_6 \cdot 3H_2O$, ≥99.5%), 2,2,6,6-tetramethylpiperidin-1-oxyl (TEMPO, 99.0%), and 5,5-dimethyl-1-pyrroline N-oxide (DMPO, 97.0%) were purchased from Aladdin Reagent Co., Ltd.

Test S2. Characterization Techniques

X-ray diffraction (XRD) measurements were conducted on a Bruker D8 diffractometer with Cu Kα radiation (λ = 0.15406 nm). Morphology and microstructure were examined using a scanning electron microscope (SEM, Regulus 8200) and a transmission electron microscope (TEM, JEM-2100). TEM samples were prepared by ultrasonically dispersing the powder in ethanol, dropping onto carbon-coated copper grids, and drying at room temperature. Aberration-corrected high-angle annular dark-field scanning TEM (HAADF-STEM) characterization was carried out on a JEM ARM200F thermal field emission microscope with a probe spherical aberration corrector. The actual Ag content in the sample was measured by an inductively coupled plasma optical emission spectrometry (ICP-OES, PerkinElmer ICP 2100). UV-visible diffuse reflectance spectra (UV-vis DRS) were recorded on an Izumi UV-3600 spectrometer equipped with a ball probe, using $BaSO_4$ as a reference, in the 400–800 nm range. X-ray photoelectron spectroscopy (XPS) was performed on a Thermo Scientific ESCA Lab250 system, calibrated with the C 1s peak at 284.8 eV. Photoluminescence (PL) spectra were acquired using a F97 Pro spectrometer, and time-resolved PL (TRPL) spectra were measured on an Edinburgh FS5 system. Photoelectrochemical properties were evaluated with a CHI660E electrochemical workstation. Electron paramagnetic resonance (EPR) spectra were obtained on a Bruker A300 at X-band frequencies, with TEMPO or DMPO as spin traps. In-situ diffuse reflection infrared Fourier transform spectroscopy (DRIFTS) was performed using a Nicolet IS50 FTIR spectrometer with a dedicated reaction chamber. Atomic force microscopy (AFM) characterization was performed using a Bruker Dimension ICON system operated in ScanAsyst mode under ambient atmospheric conditions. For sample preparation, an ultrasonicated ethanol suspension was drop-casted onto freshly cleaved mica surfaces to ensure uniform deposition.

Test S3. Photoelectrochemical Measurements

Photoelectrochemical tests were conducted using a three-electrode configuration at the Chenhua Electrochemical Station, Shanghai. An Ag/AgCl electrode served as the reference, and a platinum wire served as the counter electrode. The electrolyte was 0.2 M Na_2SO_4 aqueous solution. Parameters measured included photocurrent response, open-circuit voltage, Mott-Schottky plots, and linear sweep voltammetry. Electrochemical impedance spectroscopy (EIS) was conducted in solutions containing 0.01 M $K_3[Fe(CN)_6]/K_4[Fe(CN)_6]$ and 0.01 M KCl. The illumination source matched that used during photocatalytic experiments.

Test S4. Electron Paramagnetic Resonance (EPR) Testing

Electron paramagnetic resonance (EPR) measurements were conducted at X-band frequencies using a Bruker A300 spectrometer, with 2,2,6,6-tetramethylpyrimidin-1-oxide (TEMPO) serving as a free radical spin trap. Typically, 10 mg of the photocatalyst was dispersed in a solution containing TEMPO (0.05 mmol L^{-1}) in either aqueous or acetonitrile media to detect specific radical signals: TEMPO-e^- in water (for capturing electrons) or TEMPO-H^+ in acetonitrile (for capturing holes). The suspension was sonicated and then transferred into a capillary tube for EPR analysis. Spectra were recorded under both dark and illuminated conditions, with the light source identical to that used during photocatalytic experiments. For detecting α-hydroxybenzyl free radicals, TEMPO was replaced with 5,5-dimethyl-1-pyrroline N-oxide (DMPO), following the same procedure.

Test S5. In Situ DRIFTS Testing

In-situ diffuse reflection Fourier transform infrared spectroscopy (DRIFTS) was performed using a Nicolet IS50 FTIR spectrometer equipped with a dedicated reaction chamber. First, a dry sample was loaded into the chamber, followed by the addition of a small amount of phenylcarbinol. The chamber was sealed to remove atmospheric oxygen, then purged with argon. Subsequently, high-purity CO_2 was introduced and allowed to adsorb onto the sample surface for 30 minutes; this served as the background spectrum. Afterward, the sample was illuminated with a 300 W xenon lamp, and characteristic IR spectra were collected to monitor reaction intermediates and surface species.

Test S6. DFT calculations

Density functional theory (DFT) calculations were performed by using the Vienna ab initio simulation package (VASP) [1,2] with the Perdew-Burke-Ernzerh parameterization [3] of the

generalized gradient approximation (GGA) for the exchange correlation potential. An energy cut of 450 eV were consistently used in our calculations. A 2×2×1 Monkhorst-Pack k-point was used to sample the surface Brillouin zone. To simulate $ZnIn_2S_4$ (102) surfaces and $Ag_8/ZnIn_2S_4$ (102) system, we adopted the slab models including 6 atomic layers, in which a 20 Å of vacuum is included. During the structural optimizations, we fully relaxed atomic positions. The atomic positions were fully relaxed with the conjugate gradient procedure until the residual forces vanished within 0.02 eV/Å. The $ZnIn_2S_4$ (102), V-$ZnIn_2S_4$ (102), $Ag_8/ZnIn_2S_4$ (102), Ag_8/V-$ZnIn_2S_4$ (102) surfaces were optimized, and the relative adsorption energies Ag_8 on $ZnIn_2S_4$ (102) and V-$ZnIn_2S_4$ (102) are calculated. To explore adsorption behavior of CO_2 and CO on four different surfaces, we define adsorption energy (E_{ads}) as $E_{ads} = E_{ads/surface} - (E_{surface}+E_{ads})$. Here, $E_{surface}$ and $E_{ads/surface}$ are the total energies of surface and adsorbate (i.e. CO_2 an CO) on surface, respectively, and E_{ads} is the total energy of adsorbate. Under this definition, the more negative value stands for the more energetically stable adsorption. For the free energy profile corresponding to CO_2 dissociation, the energy of various species was calculated as described in the previously reported work [4].

Test S7. Isotopic tracing experiment

To confirm the origin of the CO product, an isotopic tracing experiment was conducted using $^{13}CO_2$ instead of CO_2 in the reaction system. The detailed procedure is as follows: 10 mg of the prepared catalyst was dispersed in a mixture consisting of 2 mL of benzyl alcohol and 8 mL of deionized water. The system was evacuated for 5 min to remove dissolved oxygen, followed by bubbling with $^{13}CO_2$. The reaction slurry was kept under continuous magnetic agitation and subjected to uniform irradiation using a 300 W Xe lamp (λ = 300-800 nm). Gas-phase products were analyzed by gas chromatography-thermal conversion-isotope ratio mass spectrometry (GC-TC-IRMS, ThermoFisher Trace1310-Delta V Advantage). A PoraPLOT Q column (25 m × 0.32 mm × 10 μm) was used, with helium as the carrier gas.

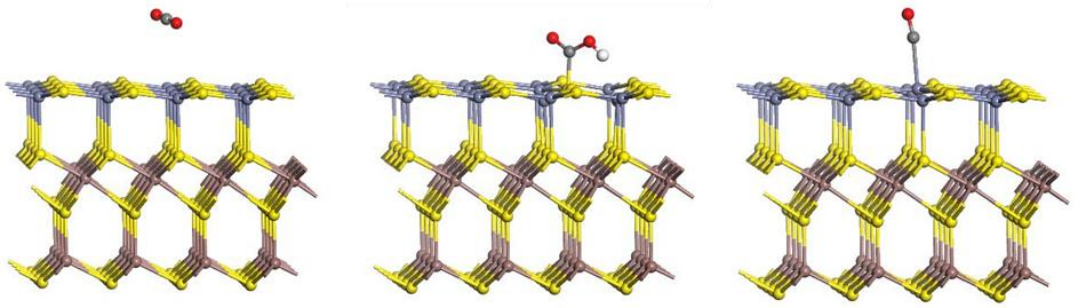


Figure S1. Side view of optimized adsorption of CO_2, COOH intermediate and CO on ZIS crystal planes (where gray, brown and yellow spheres stand for Zn, In, S atoms, respectively.).

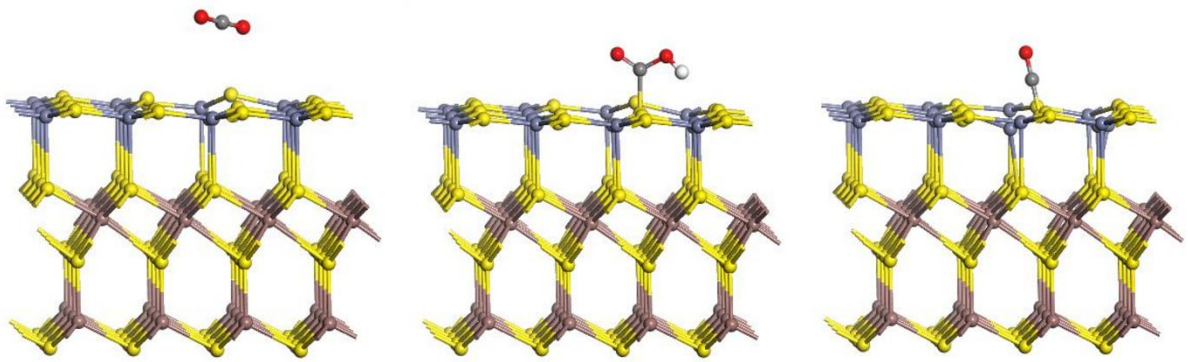


Figure S2. Side view of optimized adsorption of CO_2, COOH intermediate and CO on ZIS-V_{Zn} crystal planes (where gray, brown and yellow spheres stand for Zn, In, S atoms, respectively.).

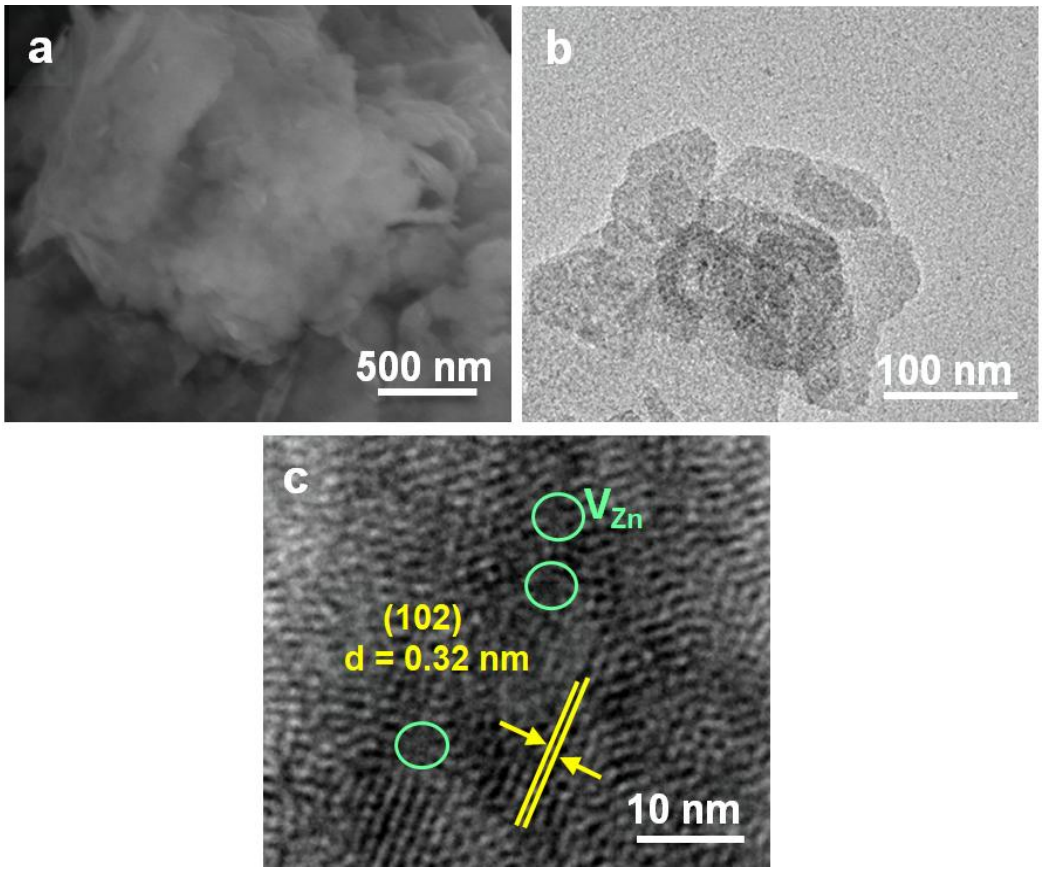


Figure S3. SEM, TEM, and HRTEM image of ZIS-V_{Zn}.

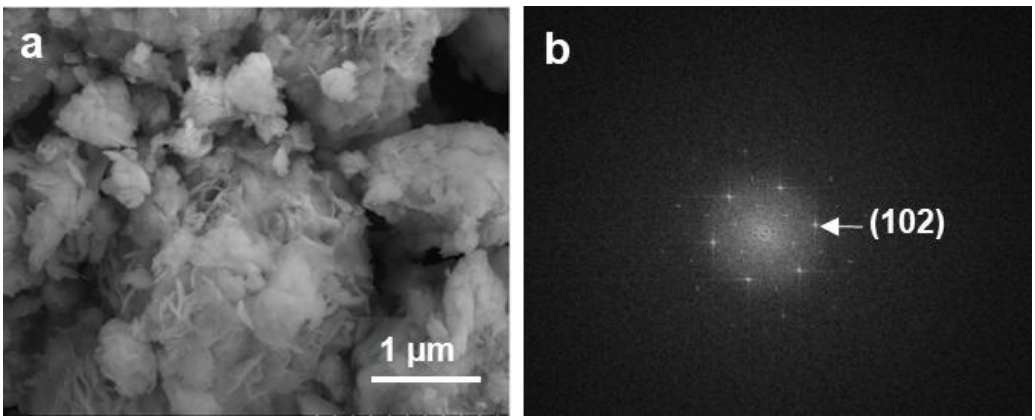


Figure S4. SEM image and SAED patterns of the optimal 1%Ag/ZIS-V_{Zn}.

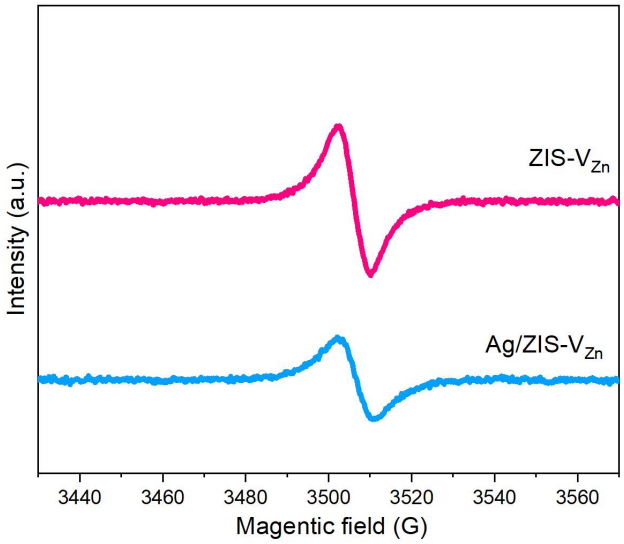


Figure S5. EPR signal of the fabricated ZIS-V_{Zn} and Ag/ZIS-V_{Zn} under liquid nitrogen temperature.

Table S1. ICP analysis of as-constructed Ag/ZIS-V_{Zn} photocatalyst.

Samples	0.5%Ag/ZIS-V_{Zn}	1%Ag/ZIS-V_{Zn}	5%Ag/ZIS-V_{Zn}	1%Ag/ZIS-V_{Zn} after reaction
Ag (wt%)	0.34%	0.83%	3.99%	0.82%

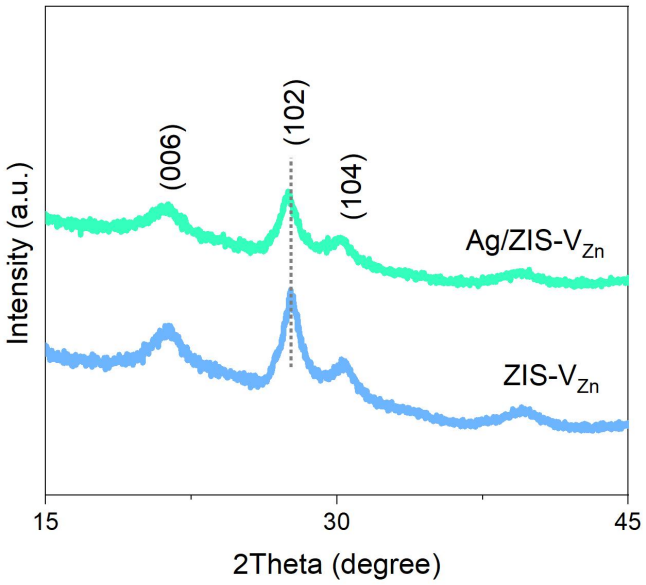


Figure S6. The XRD patterns (15 - 45°) of ZIS-V_{Zn} and Ag/ ZIS-V_{Zn}.

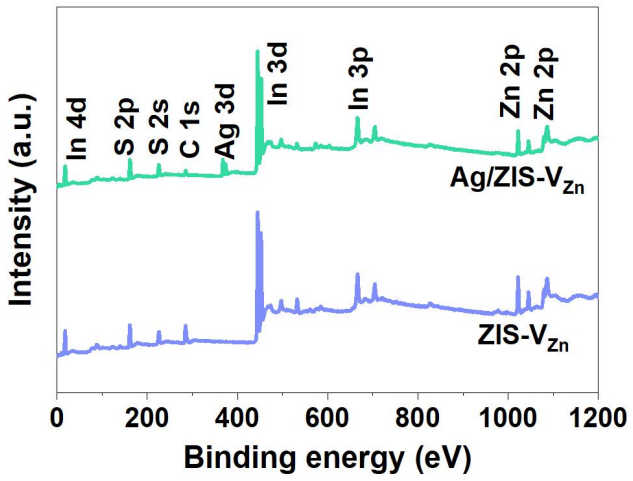


Figure S7. The XPS survey of as-constructed ZIS-V_{Zn} and Ag/ZIS-V_{Zn} catalysts.

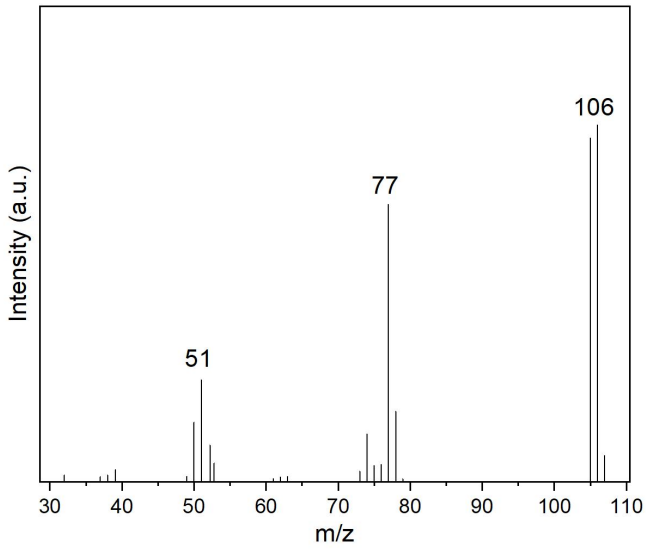


Figure S8. Mass spectrum of product benzaldehyde (BAD) via GC-MS.

As shown in Figure S8, the typical mass-to-charge ratio (m/z) values of 106.0, 77.0, and 51.0 indicate that this product is benzaldehyde.

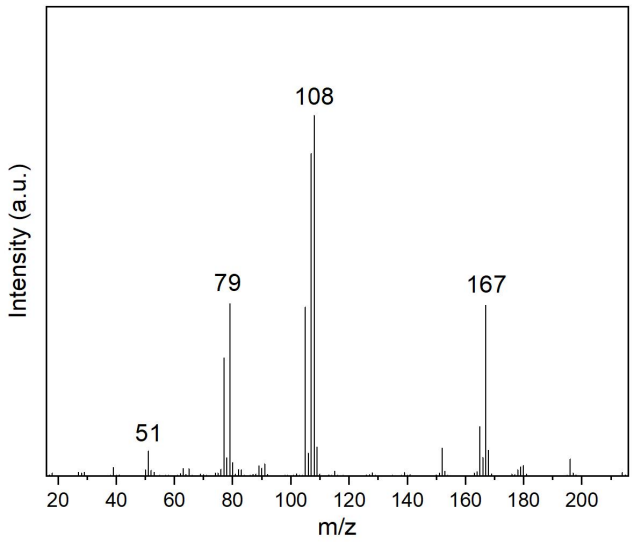


Figure S9. Mass spectrum of product hydrobenzoin (HB) via GC-MS.

As shown in Figure S9, the typical mass-to-charge ratio (m/z) values of 167, 108, 79 and 51 indicate that this product is hydrobenzoin.

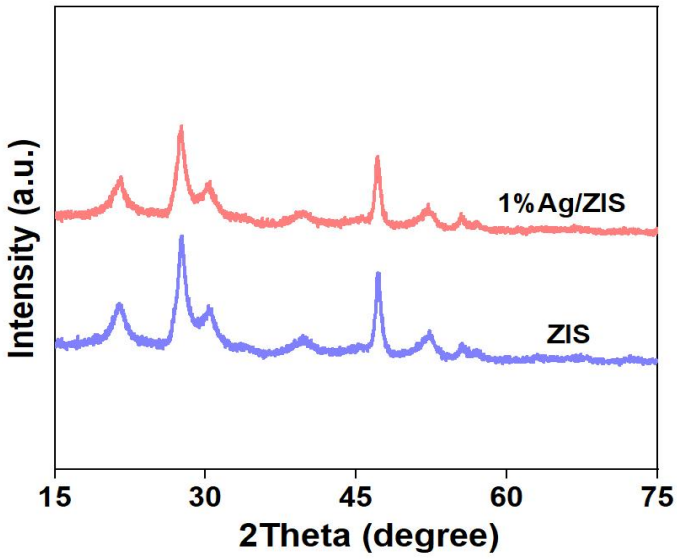


Figure 10. XRD patterns of ZIS and 1% Ag/ZIS.

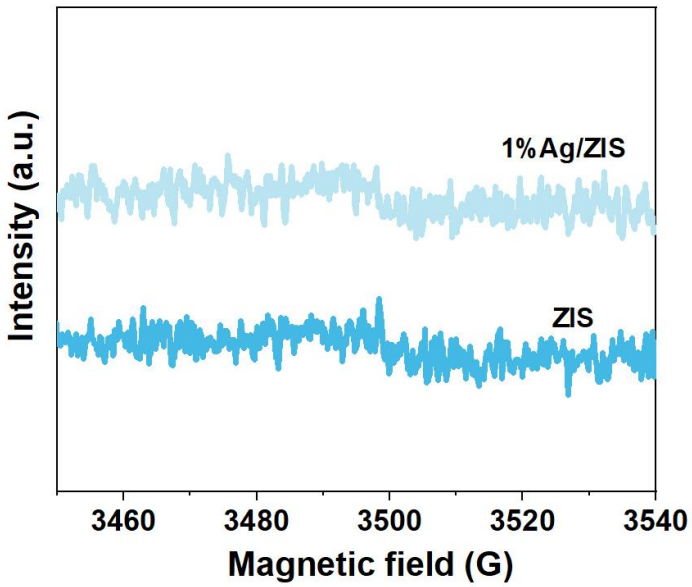


Figure S11. EPR spectra of ZIS and 1% Ag/ZIS.

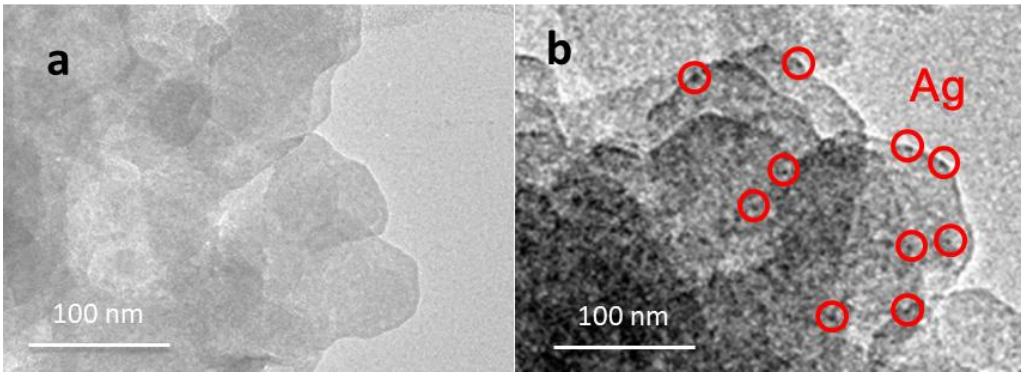


Figure S12. TEM images of (a) ZIS and (b) 1% Ag/ZIS.

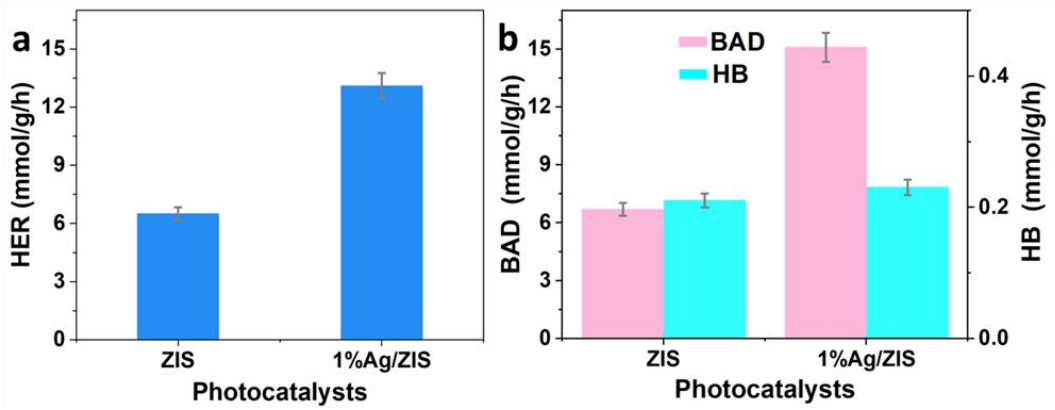


Figure S13. Dual-function photocatalysis for HER integrated with selective oxidation of phenylcarbinol over ZIS and 1% Ag/ZIS: (a) gas products and (b) liquid products.

Table S2. Comparison on photocatalytic activity for H_2 evolution over various photocatalysts

Year	Photocatalyst	Light source	substrate	H_2 evolution (mmol g^{-1} h^{-1})	Ref.
	Ag/ZIS-VZn	300W Xe lamp (λ=300-800nm)	benzyl alcohol	33.60	This work
2026	12% NiS/CZS	300W Xe lamp (λ>420nm)	benzyl alcohol	12.40	[5]
2026	$Cd_xZn_{1-x}S$	300W Xe lamp (λ>420nm)	benzyl alcohol	9.33	[6]
2026	MnO_2@$ZnIn_2S_4$@Ti_3C_2	300W Xe lamp (λ>420nm)	benzyl alcohol	6.29	[7]
2025	VDZIS/CoPPc	300W Xe lamp (λ>420nm)	benzyl alcohol	15.2	[8]
2025	$(Mn_{0.05}Cd_{0.95})_3(C_3N_3S_3)_2$/$Mn_{0.05}Cd_{0.95}S$	300W Xe lamp (λ>420nm)	benzyl alcohol	1.42	[9]
2025	V_S-ZnCoS/ZnCdS	300W Xe lamp (λ>400nm)	benzyl alcohol	27.43	[10]
2025	AIZS/NiP_x@NC	100 W LED	benzyl alcohol	9.66	[11]
2025	Pt-CdS-TBADF	300W Xe lamp (λ>420nm)	benzyl alcohol	23.38	[12]
2025	S-C_3N_4/MnCdS	300W Xe lamp (λ>420nm)	benzyl alcohol	1.50	[13]
2024	5ZIS@Ni/UN-6	300W Xe lamp (λ>420nm)	benzyl alcohol	11.44	[14]
2024	$ZnIn_2S_4$@CdS	300W Xe lamp (λ>420nm)	benzyl alcohol	12.20	[15]
2024	Cu-doped $ZnIn_2S_4$/ carbon dots	100 W LED	benzyl alcohol	45.95	[16]
2023	RuSA-RuO_2/TiO_2	300W Xe lamp	benzyl alcohol	2.91	[17]
2022	Ru/g-C_3N_{4-x}	300W Xe lamp (320nm≤λ≤850nm)	benzyl alcohol	6.42	[18]
2022	CdS−Pd SAs	300W Xe lamp (λ>420nm)	aniline benzyl alcohol	11.80	[19]
2022	ZIS/Ni_1	300W Xe lamp	benzyl alcohol	4.22	[20]
2022	CdS/WO_3-20	300W Xe lamp	benzyl alcohol	5.48	[21]

2022	NP/ZIS-O	300W Xe lamp (320nm<λ<780nm)	benzyl alcohol	15.79	[22]
2022	VC/CS-15	300W Xe lamp (λ>420nm)	benzyl alcohol	20.50	[23]
2022	$Pd_6(SR)_{12}$/CdS	300W Xe lamp (λ>400nm)	benzyl alcohol	51.67	[24]
2022	30%NiS/CdS	300W Xe lamp (λ≥420nm)	benzyl alcohol	10.39	[25]
2022	POM/ZIS	300W Xe lamp (λ>420nm)	benzyl alcohol	10.6	[26]
2021	4wt%Pt decorated 4-Cu-STO-600	300W Xe lamp (λ>420nm)	benzyl alcohol	0.62	[27]
2021	FNS@ZIS-2	300W Xe lamp (λ≥420nm)	benzyl alcohol	10.47	[28]
2021	CMCN-1	300W Xe lamp (420nm≤λ≤780nm)	benzyl alcohol	0.58	[29]
2020	C/T/MoS_2-V	300W Xe lamp (λ>420nm)	benzyl alcohol	21.40	[30]
2020	Co_9S_8/CdS	300W Xe lamp (λ≥420nm)	benzyl alcohol	61.92	[31]

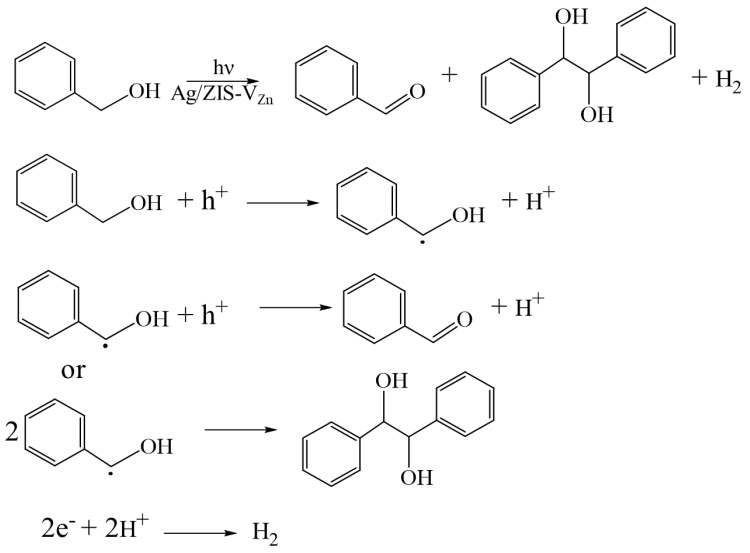


Figure S14. Reaction equations for the photocatalytic selective oxidative dehydrogenation of benzyl alcohol coupled with hydrogen production over Ag/ZIS-V_{Zn}.

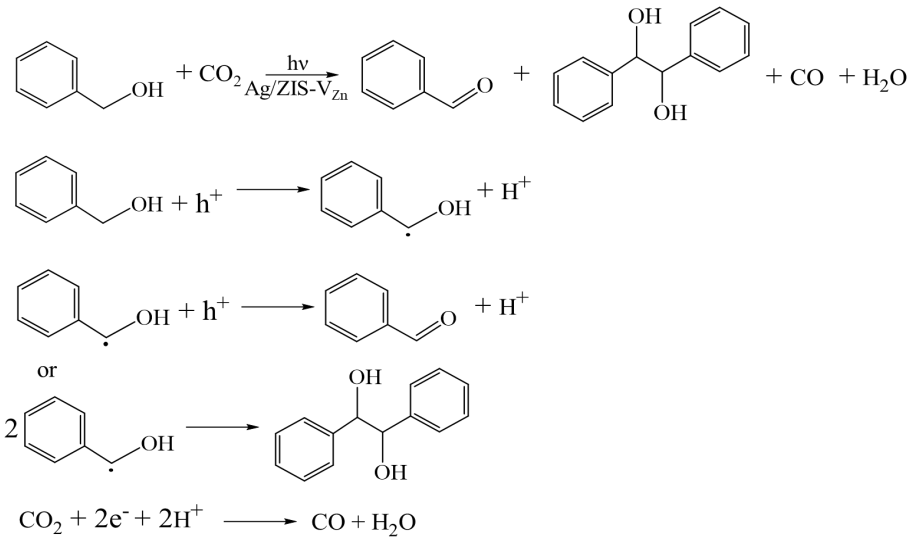


Figure S15. Reaction equations for the photocatalytic selective oxidative dehydrogenation of benzyl alcohol coupled with CO_2 reduction over Ag/ZIS-V_{Zn}.

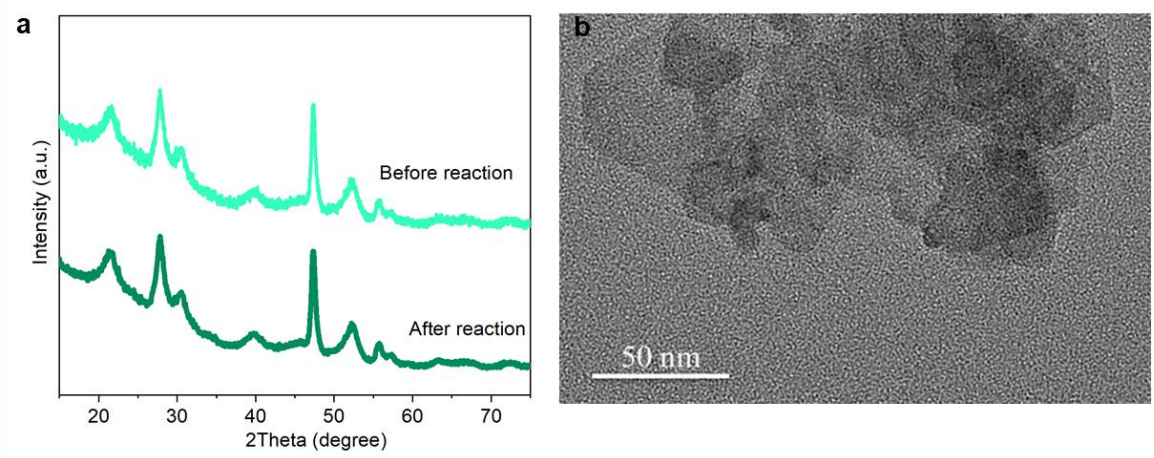


Figure S16. XRD patterns of 1%Ag/ZIS-V_{Zn} before and after reaction (a), TEM spectroscopy of used 1%Ag/ZIS-V_{Zn}.

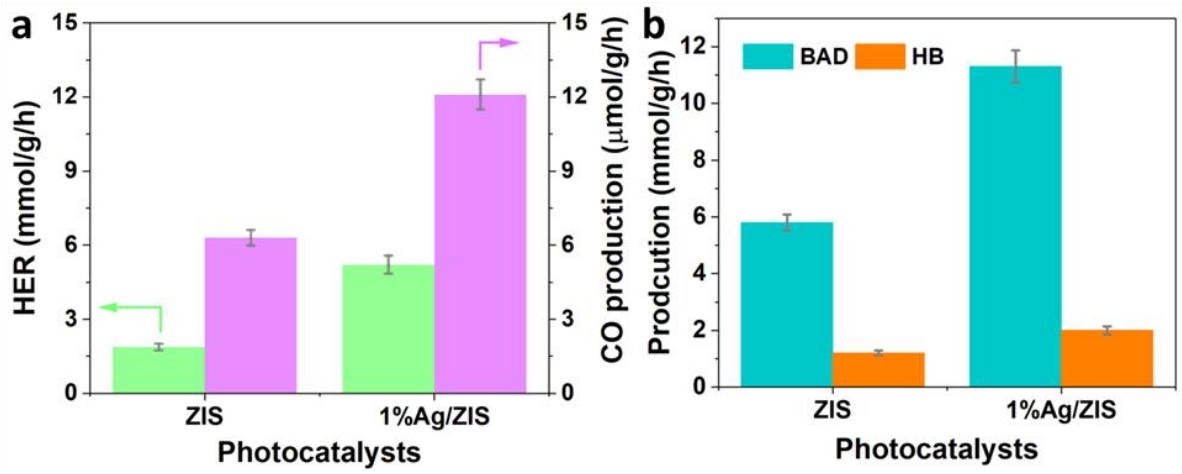


Figure S17. Synchronized photocatalysis for CO_2 reduction coupled with phenylcarbinol oxidation ZIS and 1% Ag/ZIS: (a) gas products and (b) liquid products.

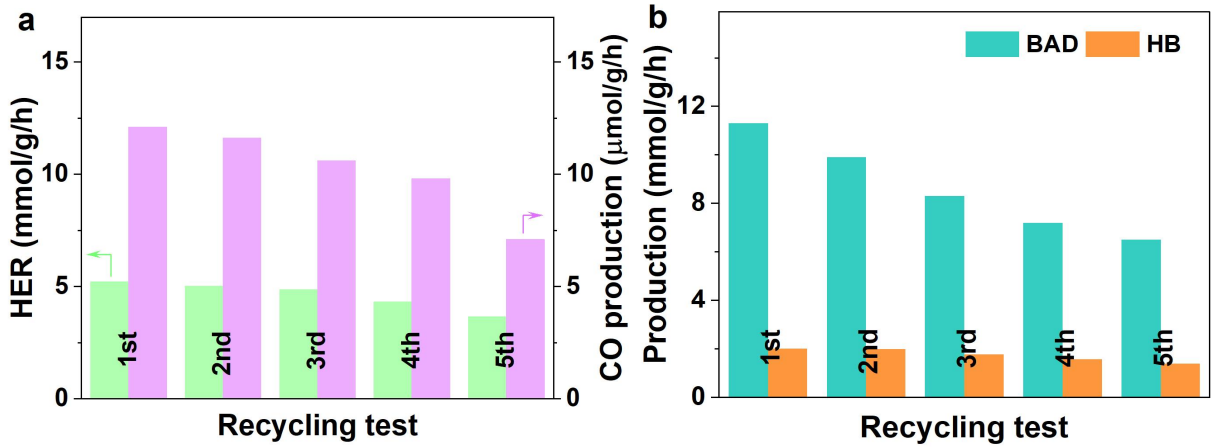


Figure S18. Cycling tests of the 1%Ag/ZIS for photocatalytic CO_2 reduction coupled with phenylcarbinol oxidation: (a) gas products and (b) liquid products.

Table S3. The controlled experiments.

Entry	Catalyst	H_2 yield (mmol/g/h)	CO yield (μmol/g/h)	BAD yield (mmol/g/h)	HB yield (mmol/g/h)
1	ZIS-V_{Zn}	13.29	6.34	3.50	19.18
2	1% Ag/ZIS-V_{Zn}	28.12	15.87	16.20	31.84
3	1% Ag/ZIS-V_{Zn}	n.d.	n.d.	n.d.	n.d.
4		n.d.	n.d.	n.d.	n.d.
5	1% Ag/ZIS-V_{Zn}	33.56	n.d.	20.24	35.10
6	1% Ag/ZIS-V_{Zn}	3.5	57.8	-	-
7	1% Ag/ZIS-V_{Zn}	0.015	1.19	-	-

1,2: 10 mg catalyst +2 mL phenylcarbinol +8 mL H_2O with CO_2 as atmosphere under illumination.

3: No illumination

4: No catalysts

5: Replace CO_2 by Ar

6: Replace phenylcarbinol by TEOA

7: Replace phenylcarbinol by H_2O

Ps: n.d. stands for that the production was been not detected.

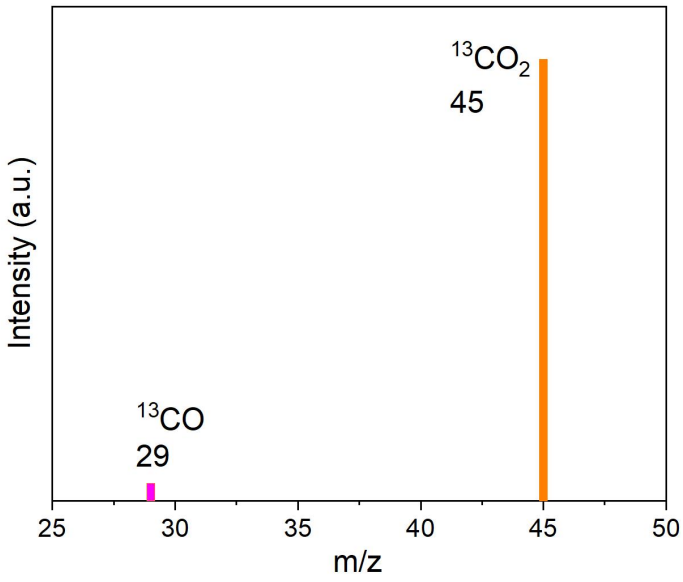


Figure S19. Mass spectra of photocatalytic reduction of $^{13}CO2$ over the optimal 1%Ag/ZIS-V_{Zn}.

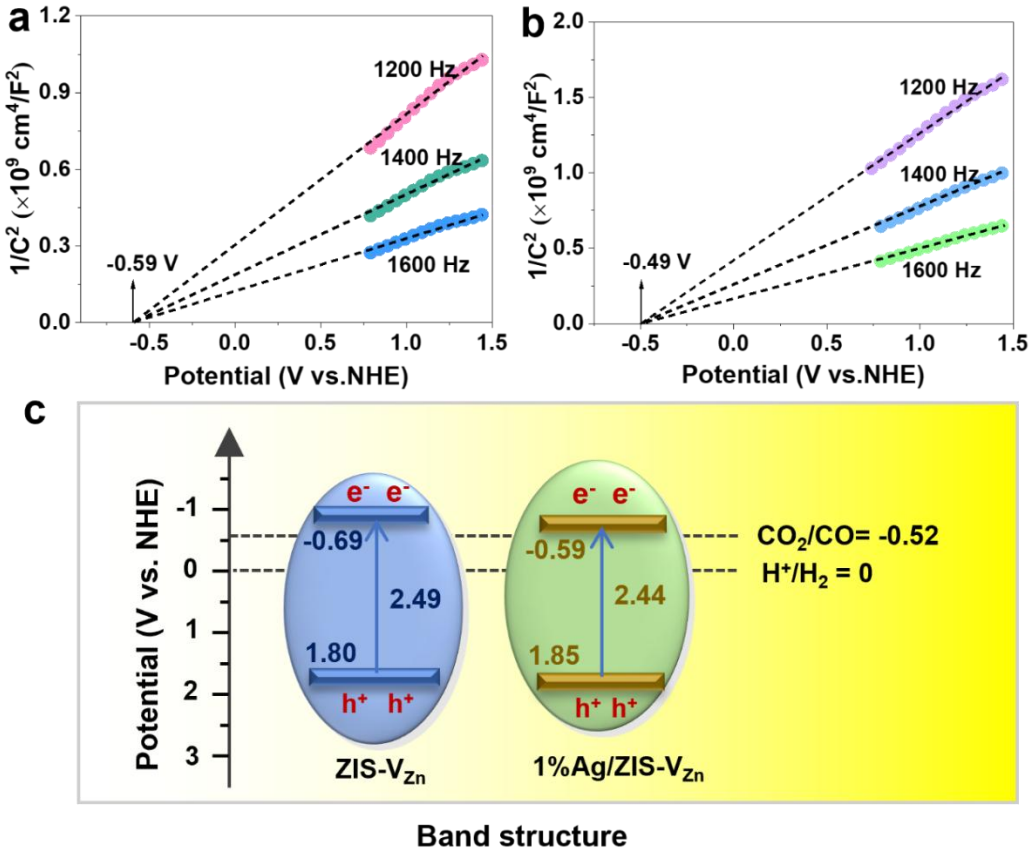


Figure S20. M-S plots of (a) ZIS-V_{Zn} and (b) 1%Ag/ZIS-V_{Zn}. (c) The band structure of ZIS-V_{Zn} and the optimal 1%Ag/ZIS-V_{Zn} catalyst.

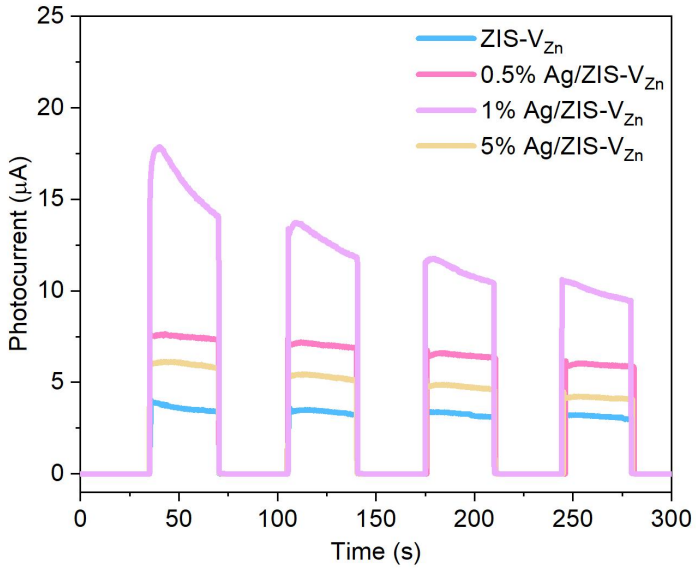


Figure S21. Transient photocurrent of Ag/ZIS-V_{zn} with various Ag loadings.

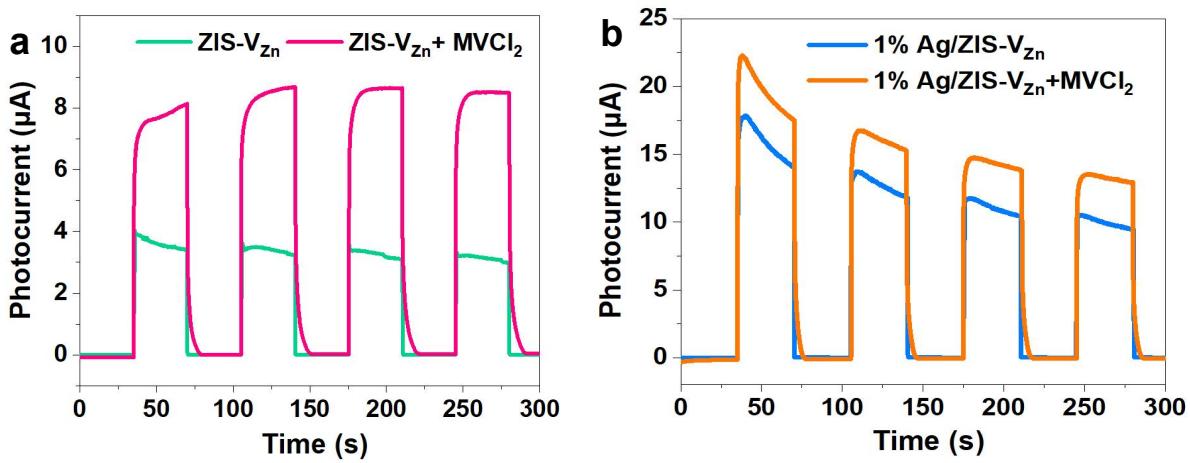


Figure S22. (a) The photocurrent response of the ZIS-V_{Zn} with the addition of $MVCl_2$. (b) The photocurrent responses of the optimal 1%Ag/ZIS catalyst with the addition of $MVCl_2$. Note: The charge transport efficiency (η_{tra}) can be evaluated by the function [32,33]: $\eta_{tra} = J_{H2O}/J_{MVCl2}$ (J_{H2O} and J_{MVCl2} are the photocurrent densities of the sample with and without $MVCl_2$, respectively).

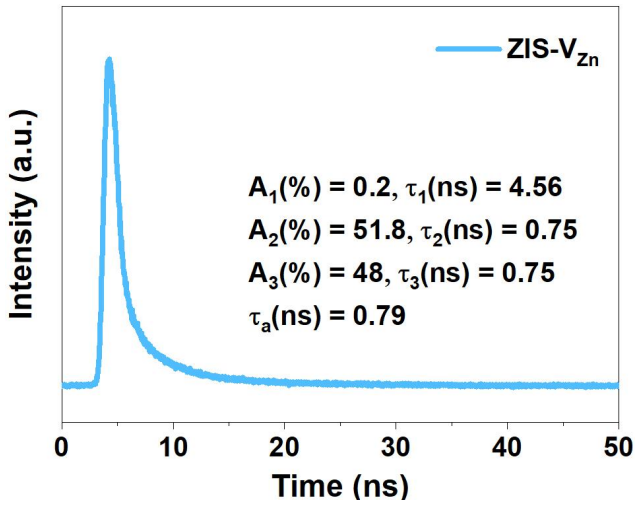


Figure S23. The fitted TRPL curve of as-fabricated (a) ZIS-V_{Zn}.

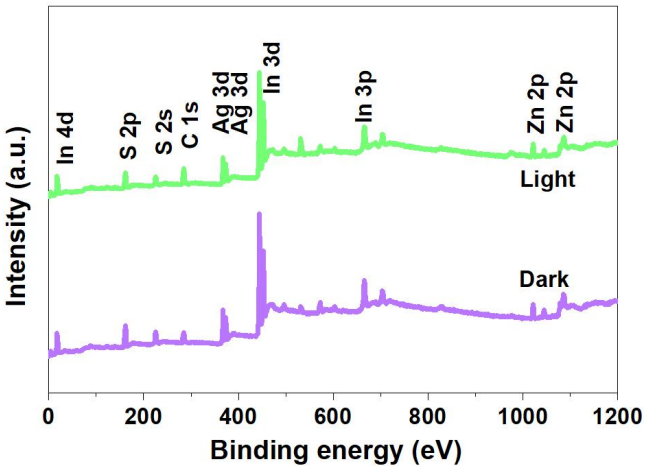


Figure S24. The XPS survey of as-constructed Ag/ZIS-V_{Zn} catalysts before and after light irradiation.

Reference

[1] G. Kresse, J. Hafner, Ab initio molecular dynamics for liquid metals, Phys. Rev. B 47 (1993) 558-561. https://doi.org/10.1103/PhysRevB.47.558.

[2] G. Kresse, D. Joubert, From ultrasoft pseudopotentials to the projector augmented-wave method, Phys. Rev. B 59 (1999) 1758-1775. https://doi.org/10.1103/PhysRevB.59.1758.

[3] G. Kresse, J. Furthmüller, Efficiency of ab-initio total energy calculations for metals and semiconductors using a plane-wave basis set, Comput. Mater. Sci. 6 (1996) 15-50. https://doi.org/10.1016/0927-0256(96)00008-0.

[4] C. Gao, Q. Meng, K. Zhao, H. Yin, D. Wang, J. Guo, S. Zhao, L. Chang, M. He, Q. Li, H. Zhao, X. Huang, Y. Gao, Z. Tang, Co_3O_4 Hexagonal Platelets with Controllable Facets Enabling Highly Efficient Visible-Light Photocatalytic Reduction of CO_2, Advanced Materials 28 (2016) 6485-6490. https://doi.org/10.1002/adma.201601387.

[5] Z. Gan, C. Ye, X. Chen, Z. Zhang, T. Ji, W. Su, Ni-MOF-74-Derived NiS/$Cd_{0.7}Zn_{0.3}S$ Boosts Photocatalytic Benzyl Alcohol Oxidation Coupled with H_2 Evolution, ACS Sustain. Chem. Eng. 14 (2026) 5100-5107. https://doi.org/10.1021/acssuschemeng.5c13785.

[6] M. Guo, Q. Xi, J. Qin, J. Liu, Y. Wang, Y. Wang, H. Li, F. Xie, C. Fan, R. Li, J. Wang, Construction of $CdxZn_{1-x}S$ for H_2 production coupled with benzyl alcohol oxidation: regulation of electrophilic and nucleophilic properties, Journal of Environmental Sciences (2026). https://doi.org/10.1016/j.jes.2026.02.024.

[7] X. Liu, X. Li, B. Sun, Y. Wu, Y. Wang, X. Sun, X. Lin, T. Gao, G. Zhou, Redox dual-cocatalysts modified $ZnIn_2S_4$ hollow sphere with spatially separated carrier for photocatalytic H_2 production coupled with selective benzyl alcohol oxidation, Sci. China Mater. 69 (2026) 1550-1561. https://doi.org/10.1007/s40843-025-3785-5.

[8] Y. Jiang, D. Hou, S. Li, S. Xiao, J. Liu, F. Lu, X.Q. Qiao, B. Sun, D.S. Li, Interfacial engineering of S-scheme $ZnIn_2S_4$/CoPPc for photoinduced H_2 production coupled with benzyl alcohol valorization, Green Chemistry 27 (2025) 14710-14720. https://doi.org/10.1039/D5GC03212A.

[9] C. You, P. Guo, B. Zhang, P. Zhang, R. Wang, Z. Zhang, S. Qiu, Novel organic-inorganic Z-scheme heterojunction for enhanced photocatalytic hydrogen evolution coupled with selective oxidation of benzyl alcohol oxidation, J. Colloid Interface Sci. 700 (2025) 138563. https://doi.org/10.1016/j.jcis.2025.138563.

[10] T.J. Siang, P. Zhang, B. Chen, W.J. Ong, Surface defect engineering of ZnCoS in ZnCdS with twin crystal structure for visible-light-driven H_2 production coupled with benzyl alcohol oxidation, Chinese Journal of Catalysis 69 (2025) 84-98. https://doi.org/10.1016/S1872-2067(24)60197-X.

[11] T. Ren, Q. Chen, Y. Liu, A.U. Khan, D. Zhang, J. Li, L. Li, H. Lin, N. Liu, B. Mao, N-Doped Carbon Layer Encapsulated NiP_x for Photocatalytic Alcohol Oxidation Coupled Hydrogen Evolution on Ag–In–Zn–S Quantum Dots, Inorg. Chem. 64 (2025) 4447-4460. https://doi.org/10.1021/acs.inorgchem.4c05199.

[12] B. Feng, B. Qi, S. Wang, P. Zhang, R. Shen, Y. Li, X. Li, Elucidating the Charge-Separation and Oxidation Dynamics in Fluorenone-COF/CdS S-Scheme Heterojunction for Photocatalytic Benzaldehyde and Hydrogen Production, ENERGY & ENVIRONMENTAL MATERIALS 9 (2026) e70153. https://doi.org/10.1002/eem2.70153.

[13] P. Guo, X. Liu, C. You, B. Zhang, P. Zhang, Z. Xiong, H. Li, H. Zhang, R. Wang, Z. Zhang, S. Qiu, Controllable construction of defect-mediated Z-scheme heterojunction for dual-functional cooperative photocatalysis of benzyl alcohol conversion and hydrogen evolution, Applied Catalysis B: Environment and Energy 366 (2025) 125011. https://doi.org/10.1016/j.apcatb.2024.125011.

[14] Z. Jia, R. Li, P. Ji, Z. Xu, K.P. Homewood, X. Xia, Y. Gao, J.P. Zou, X. Chen, Design and fabrication of a novel 2D/3D $ZnIn_2S_4$@Ni1/UiO-66-NH_2 heterojunction for highly efficient

visible-light photocatalytic H2 evolution coupled with benzyl alcohol valorization, Applied Catalysis B: Environment and Energy 357 (2024) 124279. https://doi.org/10.1016/j.apcatb.2024.124279.

[15] L. Yang, J. Guo, S. Chen, A. Li, J. Tang, N. Guo, J. Yang, Z. Zhang, J. Zhou, Tailoring the catalytic sites by regulating photogenerated electron/hole pairs separation spatially for simultaneous selective oxidation of benzyl alcohol and hydrogen evolution, J. Colloid Interface Sci. 659 (2024) 776-787. https://doi.org/10.1016/j.jcis.2024.01.022.

[16] Q. Chen, B. Mao, Y. Liu, Y. Zhou, H. Huang, S. Wang, L. Li, W.C. Yan, W. Shi, Z. Kang, Designing 2D carbon dot nanoreactors for alcohol oxidation coupled with hydrogen evolution, Nat. Commun. 15 (2024) 8052. https://doi.org/10.1038/s41467-024-52406-2.

[17] B. Xing, T. Wang, Z. Zheng, S. Liu, J. Mao, C. Li, B. Li, Synchronous fabrication of Ru single atoms and RuO_2 on hierarchical TiO_2 spheres for enhanced photocatalytic coproduction of H_2 and benzaldehyde, Chemical Engineering Journal 461 (2023) 141871. https://doi.org/10.1016/j.cej.2023.141871.

[18] Q. Yang, T. Wang, Z. Zheng, B. Xing, C. Li, B. Li, Constructing interfacial active sites in Ru/g-C_3N_{4-x} photocatalyst for boosting H_2 evolution coupled with selective benzyl-alcohol oxidation, Appl. Catal. B 315 (2022) 121575. https://doi.org/10.1016/j.apcatb.2022.121575.

[19] F. Niu, W. Tu, X. Lu, H. Chi, H. Zhu, X. Zhu, L. Wang, Y. Xiong, Y. Yao, Y. Zhou, Z. Zou, Single Pd–Sx Sites In Situ Coordinated on CdS Surface as Efficient Hydrogen Autotransfer Shuttles for Highly Selective Visible-Light-Driven C–N Coupling, ACS Catal. 12 (2022) 4481-4490. https://doi.org/10.1021/acscatal.2c00433.

[20] J.Y. Li, M.Y. Qi, Y.J. Xu, Efficient splitting of alcohols into hydrogen and C–C coupled products over ultrathin Ni-doped $ZnIn_2S_4$ nanosheet photocatalyst, Chinese Journal of Catalysis 43 (2022) 1084–1091. https://doi.org/10.1016/S1872-2067(21)63931-1.

[21] Y.L. Wu, M.Y. Qi, C.L. Tan, Z.R. Tang, Y.J. Xu, Photocatalytic selective oxidation of aromatic alcohols coupled with hydrogen evolution over CdS/WO_3 composites, Chinese Journal of Catalysis 43 (2022) 1851-1859. https://doi.org/10.1016/S1872-2067(21)63989-X.

[22] J. Wan, L. Liu, Y. Wu, J. Song, J. Liu, R. Song, J. Low, X. Chen, J. Wang, F. Fu, Y. Xiong, Exploring the Polarization Photocatalysis of $ZnIn_2S_4$ Material toward Hydrogen Evolution by Integrating Cascade Electric Fields with Hole Transfer Vehicle, Adv. Funct. Mater. 32 (2022)

2203252. https://doi.org/10.1002/adfm.202203252.

[23] M. Tayyab, Y. Liu, S. Min, R. Muhammad Irfan, Q. Zhu, L. Zhou, J. Lei, J. Zhang, Simultaneous hydrogen production with the selective oxidation of benzyl alcohol to benzaldehyde by a noble-metal-free photocatalyst VC/CdS nanowires, Chinese Journal of Catalysis 43 (2022) 1165-1175. https://doi.org/10.1016/S1872-2067(21)63997-9.

[24] D. Luo, Y. Luo, X. Lu, M. Shi, J. Wei, Z. Lu, Y. Huang, Y. Ni, Cooperative selective benzyl alcohol oxidation and hydrogen production over $Pd_6(SC_{12}H_{25})_{12}$ cluster-coupled CdS nanorods: the key role of water in photocatalytic benzyl alcohol splitting, J. Mater. Chem. A Mater. 10 (2022) 15941-15948. https://doi.org/10.1039/D2TA04073E.

[25] J. Luo, M. Wang, L. Chen, J. Shi, Efficient benzaldehyde photosynthesis coupling photocatalytic hydrogen evolution, Journal of Energy Chemistry 66 (2022) 52-60. https://doi.org/10.1016/j.jechem.2021.07.017.

[26] F. Xing, R. Zeng, C. Cheng, Q. Liu, C. Huang, POM-incorporated $ZnIn_2S_4$ Z-scheme dual-functional photocatalysts for cooperative benzyl alcohol oxidation and H_2 evolution in aqueous solution, Appl. Catal. B 306 (2022) 121087. https://doi.org/10.1016/j.apcatb.2022.121087.

[27] B. Li, J. Hong, Y. Ai, Y. Hu, Z. Shen, S. Li, Y. Zou, S. Zhang, X. Wang, G. Zhao, X. Xu, Visible-near-infrared-light-driven selective oxidation of alcohols over nanostructured Cu doped $SrTiO_3$ in water under mild condition, J. Catal. 399 (2021) 142-149. https://doi.org/10.1016/j.jcat.2021.05.008.

[28] L. Zhong, B. Mao, M. Liu, M. Liu, Y. Sun, Y.T. Song, Z.M. Zhang, T.B. Lu, Construction of hierarchical photocatalysts by growing $ZnIn_2S_4$ nanosheets on Prussian blue analogue-derived bimetallic sulfides for solar co-production of H_2 and organic chemicals, Journal of Energy Chemistry 54 (2021) 386-394. https://doi.org/10.1016/j.jechem.2020.06.001.

[29] H. Wang, J. Zhang, X. Jin, X. Wang, F. Zhang, J. Xue, Y. Li, J. Li, G. Zhang, General surface grafting strategy-derived carbon-modified graphitic carbon nitride with largely enhanced visible light photocatalytic H_2 evolution coupled with benzyl alcohol oxidation, J. Mater. Chem. A Mater. 9 (2021) 7143-7149. https://doi.org/10.1039/D1TA00142F.

[30] M.Y. Qi, Y. H. Li, F. Zhang, Z.R. Tang, Y. Xiong, Y.J. Xu, Switching Light for Site-Directed Spatial Loading of Cocatalysts onto Heterojunction Photocatalysts with Boosted Redox Catalysis,

ACS Catal. 10 (2020) 3194-3202. https://doi.org/10.1021/acscatal.9b05420.

[31] M. Liu, L.Z. Qiao, B.B. Dong, S. Guo, S. Yao, C. Li, Z.M. Zhang, T.B. Lu, Photocatalytic coproduction of H_2 and industrial chemical over MOF-derived direct Z-scheme heterostructure, Appl. Catal. B 273 (2020) 119066. https://doi.org/10.1016/j.apcatb.2020.119066.

[32] M.S. Bootharaju, C.W. Lee, G. Deng, H. Kim, K. Lee, S. Lee, H. Chang, S. Lee, Y.-E. Sung, J. S. Yoo, N. Zheng, T. Hyeon, Atom-Precise Heteroatom Core-Tailoring of Nanoclusters for Enhanced Solar Hydrogen Generation, Adv. Mater. 35 (2023) 2207765. https://doi.org/10.1002/adma.202207765.

[33] J. Lei, H. Yang, B. Weng, Y.-M. Zheng, S. Chen, P.W. Menezes, S. Meng, Optimization of Adsorption Sites for Selective Hydrobenzoin and Syngas Production in a Single Photoredox Cycle, Adv. Energy Mater. 15 (2025) 2500950. https://doi.org/10.1002/aenm.202500950.